# Impact of the dose quantity used in MV photon optimization on dose distribution, robustness and complexity

Short running Title: Dose quantity in MV photon optimization

Diego Jurado-Bruggeman
*Medical Physics and Radiation Protection Department, Institut Català d'Oncologia, Avda. França sn, 17007, Girona, Spain*

Carles Muñoz-Montplet
*Medical Physics and Radiation Protection Department, Institut Català d'Oncologia, Avda. França sn, 17007, Girona, Spain*
*Department of Medical Sciences, University of Girona, C/Emili Grahit 77, 17003 Girona, Spain*

Victor Hernandez
*Department of Medical Physics, Hospital Universitari Sant Joan de Reus, IISPV, Tarragona, Spain*

Jordi Saez
*Department of Radiation Oncology, Hospital Clínic de Barcelona, Spain*

Rafael Fuentes-Raspall
*Radiation Oncology Department, Institut Català d'Oncologia, Avda. França s/n, 17007 Girona, Spain*
*Department of Medical Sciences, University of Girona, C/Emili Grahit 77, 17003 Girona, Spain*

Corresponding author:
Diego Jurado-Bruggeman
Medical Physics and Radiation Protection Department
Institut Català d'Oncologia
Avda. França sn, 17007, Girona, Spain
Email: djurado@iconcologia.net – Telephone: (+34) 972 28 50 30

## Abstract

**Purpose:** Convolution/superposition algorithms used in MV photon radiotherapy model radiation transport in water, yielding dose to water-in-water ($D_{w,w}$). Advanced algorithms constitute a step forward, but their dose distributions in terms of dose to medium-in-medium ($D_{m,m}$) or dose to water-in-medium ($D_{w,m}$) can be problematic when used in plan optimization due to their different dose responses to some atomic composition heterogeneities. Failure to take this into account can lead to undesired overcorrections and thus to unnoticed suboptimal and unrobust plans. Dose to reference-like medium ($D_{ref,m*}$) was recently introduced to overcome these limitations while ensuring accurate transport. This work evaluates and compares the performance of these four dose quantities in PTV-based optimization.

**Methods:** We considered three cases with heterogeneities inside the PTV: virtual phantom with water surrounded by bone; head and neck; and lung. These cases were planned with VMAT technique, optimizing with the same setup and objectives for each dose quantity. We used different algorithms of the Varian Eclipse treatment planning system (TPS): Acuros XB for $D_{m,m}$ and $D_{w,m}$, and AAA for $D_{w,w}$. $D_{ref,m*}$ was obtained from $D_{m,m}$ distributions using an in-house software considering water as the reference medium ($D_{w,m*}$). The optimization process consisted of: (1) common first optimization, (2) dose distribution computed for each quantity, (3) re-optimization, (4) final calculation for each dose quantity. The dose distribution, robustness to patient setup errors, and complexity of the plans were analyzed and compared.

**Results:** The quantities showed similar dose distributions after the optimization but differed in terms of plan robustness. The cases with soft tissue and high-density heterogeneities followed the same pattern. For AXB $D_{m,m}$, cold regions appeared in the heterogeneities after the first optimization. They were compensated in the second optimization through local fluence increases, but any positional mismatch impacted robustness, with CTV variations from the nominal scenario around +3% for bone and up to +7% for metal. For AXB $D_{w,m}$ the pattern was

inverse (hot regions compensated by fluence decreases) and more pronounced, with CTV dose variations around -7% for bone and up to -17% for metal. Neither AXB $D_{w,m*}$ nor AAA $D_{w,w}$ presented these dose inhomogeneities, which resulted in more robust plans. However, $D_{w,w}$ differed markedly from the other quantities in the lung case because of its lower radiation transport accuracy. AXB $D_{m,m}$ was the most complex of the four dose quantities and AXB $D_{w,m*}$ the least complex, though we observed no major differences in this regard.

**Conclusions:** The dose quantity used in MV photon optimization can affect plan robustness. $D_{w,w}$ distributions from convolution/superposition algorithms are robust but may not provide sufficient radiation transport accuracy in some cases. $D_{m,m}$ and $D_{w,m}$ from advanced algorithms can compromise robustness because their different responses to some composition heterogeneities introduce additional fluence compensations. $D_{ref,m*}$ offers advantages in plan optimization and evaluation, producing accurate and robust plans without increasing complexity. $D_{ref,m*}$ can be easily implemented as a built-in feature of the TPS and can facilitate and simplify the treatment planning process when using advanced algorithms. Final reporting can be kept in $D_{m,m}$ or $D_{w,m}$ for clinical correlations.

**Key words:** optimization, dose-to-reference-like medium, dose-to-water, dose-to-medium, robustness

## 1. INTRODUCTION

Dose calculation accuracy is crucial in radiotherapy. It should be within 2-3% globally, with a 1-2% goal for heterogeneities and systematic issues.[1–4] However, differences between dose calculation algorithms and/or the clinical dose quantity used may result in differences that exceed the desired accuracy in some situations.

Modern calculation algorithms for MV photon beams can be roughly classified into convolution/superposition (C/S) and advanced groups. In general, C/S algorithms model radiation transport in water-like tissues and consider heterogeneities to be water of different electron densities; hence the dose distribution is reported in terms of absorbed dose to water surrounded by water ($D_{w,w}$). These algorithms offer satisfactory accuracy globally, but it can diminish in the presence of heterogeneities.[3,5,6] Advanced algorithms, based on Monte Carlo (MC) or the linear Boltzmann transport equation (LBTE), model the physics of radiation transport in any media. MC algorithms simulate the random trajectories of individual particles while LBTE describes radiation transport macroscopically.[7,8] In these algorithms, voxel doses can be reported as water voxels surrounded by medium ($D_{w,m}$) or medium voxels surrounded by medium ($D_{m,m}$). Advanced algorithms have overcome most of the issues of C/S algorithms, and their use is explicitly recommended when their performance is notably superior.[9–11]

Doses to water-like tissues derived from advanced algorithms are similar to those from C/S algorithms, but for tissues like bone or, to a lesser extent, adipose tissue, the discrepancies can exceed the accuracy target.[12] Cortical bone represents the most extreme case, where differences between $D_{w,m}$ and $D_{m,m}$ can exceed 14%, and differences between $D_{w,m}$ and $D_{w,w}$ can be as high as 10%-11%.[12,13] Each quantity has its advocates, and clinical trials, protocols, and guidelines contain mixed recommendations on whether to choose $D_{m,m}$[14,15] or $D_{w,m}$,[9,16] although the consensus seems to be moving towards $D_{m,m}$ to maximize consistency.[15,17] Consequently, multiple dose quantities are used in clinical practice, each with its own particular strengths and weaknesses.

Regarding plan optimization, dose distribution calculation and evaluation drive the iterative process in which the photon fluence is optimized to achieve a set of planning goals. Though most systems, for

reasons of efficiency, currently use C/S algorithms during the optimization process, technological improvements might soon enable plan optimization based on advanced algorithms. However, their use introduces new challenges in the treatment planning process since their dose values are sensitive to both medium composition and dose reporting mode. This makes it difficult to determine whether any failure to meet particular goals is due to a suboptimal plan or rather to the impact of atomic composition heterogeneities on the calculated dose. Using advanced algorithm-derived quantities in dose optimization therefore entails a risk of forcing undesired overcorrections, leading to unnoticed suboptimal and unrobust plans.[18] This is particularly relevant in automated planning, where these factors should be accounted for in the automation algorithm or the machine learning model. In addition, $D_{m,m}$ and $D_{w,m}$ produce opposite effects for most materials, which can lead to inconsistent decisions, competing overcorrections, and ultimately to patients receiving different doses.

Sterpin illustrated these potential dangers for PTV-based optimization in terms of $D_{m,m}$ by delivering a uniform dose to a virtual case that included bone.[18] If an algorithm yielding $D_{w,w}$ is used for optimization (where medium is considered to be water) and charged particle equilibrium (CPE) exists, this is accomplished by uniform photon distribution as the dose values are then insensitive to density in accordance with Fano's theorem.[19,20] With $D_{m,m}$ optimization, on the other hand, differing dose responses to the same incident fluence distribution in some medium heterogeneities within the PTV can lead to dose inhomogeneities, which must then be compensated by local changes in the photon fluence. These undesired local fluence variations could increase plan complexity and, more importantly, compromise GTV/CTV doses in the presence of geometric errors.

The solutions proposed by Sterpin to address these drawbacks when optimizing with $D_{m,m}$ were either to use robust optimization or to force all tissues in the PTV to match tumor composition while keeping the correct electron density. These strategies have their merits but also shortcomings. Robust optimization provides a comprehensive and optimal solution to the problem. However, it is not available for photons in most treatment planning systems (TPS) and increases optimization time especially when combined with advanced dose calculation algorithms. The second proposal could undermine the radiation transport advantages of advanced algorithms if the PTV contains elements

that interact with radiation differently than the tumor, as this would affect attenuation and dispersion (e.g., higher photon interaction cross sections for high-Z elements in cortical bone, metal implants, or prosthesis).[11,21]

In this context, a new dose quantity, the dose to reference-like medium ($D_{ref,m*}$), was recently introduced to evaluate and optimize MV photon plans when using advanced algorithms.[22] $D_{ref,m*}$ has the strengths of both advanced and C/S calculation algorithms, i.e., accurate radiation transport in medium and dose values less sensitive to composition heterogeneities. Furthermore, the dose distribution in terms of $D_{ref,m*}$ can be easily derived from the dose distribution given by advanced algorithms.[22] Plan optimization with $D_{ref,m*}$ has yet to be investigated, but it could potentially overcome the shortcomings detailed above when optimizing with advanced algorithms to obtain accurate, consistent, more robust, and less complex plans.

This study examines the impact of the dose quantity used in PTV-based optimization of MV photon plans ($D_{w,w}$ from C/S, $D_{m,m}$, $D_{w,m}$, $D_{ref,m*}$) on three different outcomes: (1) the quality of the resulting dose distribution; (2) plan robustness to geometric errors; (3) plan complexity. The whole study was performed in a clinical scenario, optimizing representative cases with each of the four dose quantities.

## 2. MATERIALS AND METHODS

### 2.A. Dose quantities

In this subsection we will briefly describe the dose quantities used and their differences. For photon radiation and under δ-ray equilibrium conditions, the absorbed dose in a voxel (D) corresponds to the energy lost by primary charged particles in its mass.[23] In the general case that the surrounding medium (sm) is different from that of the voxel (vm), the absorbed dose ($D_{sm,vm}$) is given by:

$$D_{sm,vm} \overset{\delta-eq}{=} \int_0^{E_{max}} \Phi_{E,\mathrm{sm}}^{prim} \left[\frac{S_{el}(E)}{\rho}\right]_{vm} dE \#(1)$$

where $\Phi_{E,sm}^{prim}$ is the primary electron fluence differential in energy in the surrounding medium for each energy $E$ ranging from 0 to the maximum energy $E_{max}$, and $[S_{el}(E)/\rho]_{vm}$ is the mass electronic (collision) stopping power of the voxel's medium. This expression shows why different radiation transport modeling and combinations of surrounding and voxel media can return different dose values: photon and electron radiation transport to the voxel affects $\Phi_{E,sm}^{prim}$; different surrounding media can present different radiation-medium interactions resulting in different $\Phi_{E,sm}^{prim}$; and $[S_{el}(E)/\rho]_{vm}$ depends on the voxel's medium.

The different calculation algorithms handle radiation transport and dose deposition differently.[15] Regarding radiation transport, differences are inherently higher across C/S algorithms as each one uses its own approach, while advanced algorithms model the physics involved more accurately and, consequently, their variability is lower. There are also differences between algorithms in the media used to perform the transport and report the doses. Most C/S algorithms transport in water and report $D_{w,w}$, but the collapsed cone algorithm can transport in medium and yield $D_{m,m}$ if the attenuation coefficients of the different media are used.[15,24] Advanced algorithms inherently transport radiation through the medium and report $D_{m,m}$ or $D_{w,m}$ (in MC, by post-processing $D_{m,m}$ using stopping power ratios); but in ViewRay MC, all materials are defined as water of different densities and $D_{m,m}$ turns into $D_{w,w}$.[15,17] Therefore, when characterizing dose distributions, transport accuracy and dose deposition characteristics are mixed, and it is relevant to specify both the dose quantities and the type of algorithm.

We evaluated four different dose quantities: dose to medium-in-medium ($D_{m,m}$), dose to water-in-medium ($D_{w,m}$), and dose to reference-like medium ($D_{ref,m*}$) from advanced algorithms; and dose to water-in-water ($D_{w,w}$) from C/S algorithms. Three are clinically available ($D_{m,m}$, $D_{w,m}$, and $D_{w,w}$), while $D_{ref,m*}$ was recently proposed for plan optimization and evaluation when using advanced algorithms.[22] These dose concepts are illustrated in Fig. 1.

The $D_{ref,m*}$ is based on radiation transport in media using advanced algorithms, and is linked to a reference medium (ref). The rationale behind $D_{ref,m*}$ is to obtain dose distributions like those of $D_{m,m}$ and $D_{w,m}$ but without their different response in some atomic composition heterogeneities. In accordance with Fano's theorem, this requires uniform atomic composition since, then, dose values are insensitive to density where CPE is established. The atomic composition is that of the reference medium everywhere, but the media surrounding the voxel must keep the actual radiation transport. Therefore, $D_{ref,m*}$ is defined as the absorbed dose in a voxel made of this reference medium surrounded by a reference-like medium (m*) with the same radiation transport characteristics as the actual medium.[22] This can be expressed as:

$$D_{ref,m*} \overset{\delta-eq}{=} \int_0^{E_{max}} \Phi_{E,m*}^{prim} \left[\frac{S_{el}(E)}{\rho}\right]_{ref} dE \#(2)$$

This definition ensures accurate radiation transport in medium since an advanced algorithm is used and, by definition, the reference-like medium preserves the attenuation and dispersion of the actual medium. The surrounding reference-like medium also provides the secondary electron fluence in the voxel as if its atomic composition matched the voxel's reference medium, thus compensating (adding or removing) any discrepancies in particle fluence and spectrum introduced by non-reference-like media. $D_{ref,m*}$ is conceptually different from $D_{w,w}$ since radiation transport is not modified even when materials that interact with radiation differently than water are present (e.g., photoelectric effect and pair production in high-Z elements).

$D_{ref,m*}$ is not related to any radiobiological consideration, nor to the 'true' dose received by the voxels ($D_{m,m}$)[13,25] or the target cells ($D_{w,m}$)[9,25,26]. $D_{ref,m*}$ is useful to connect with the clinical data collected through previous algorithms and offers several advantages for planning and evaluation that will be shown in the sections that follow.

## 2.B. Computation of $D_{ref,m*}$ distributions

In this study, we considered water as the reference medium to be consistent with the dose definition from which historical clinical data were obtained. We will therefore refer to $D_{ref,m*}$ as $D_{w,m*}$. All the rationale presented for water can be applied to whichever reference medium is chosen, e.g. muscle when following the AAPM TG-329 guidelines.[15]

$D_{w,m*}$ distributions can be obtained by post-processing $D_{w,m}$ or $D_{m,m}$ distributions, applying a correction factor (CF) to each voxel corresponding to the ratio of $D_{w,m*}$ to $D_{m,m}$ or $D_{w,m}$.[22] The original distributions from advanced algorithms ensure accurate radiation transport, while the CF compensates any differences in particle fluence and spectrum introduced by non-water-like media. This CF depends on the voxel's atomic composition, the beam spectrum, and the original dose reporting mode.

The CFs for a given medium *m* and beam can be derived using dosimetric principles and basic quantities. An approach based on cavity theory cannot be used because it is not only the medium of a single voxel that is changed to water, but also the whole surrounding medium that is changed to water-like medium. However, the ratio of $D_{w,m*}$ to $D_{m,m}$ matches the ratio of collision kerma for both media if transient charged-particle equilibrium exists and their radiative fractions are neglected or equal. Hence, the CF for $D_{m,m}$ is: [22,27]

$$CF_{m,D_{m,m}}^{beam} = \frac{D_{w,m*}}{D_{m,m}} = \left[\frac{\overline{\mu_{en}}}{\rho}\right]_{w,m} \quad \#(3)$$

where $[\overline{\mu_{en}}/\rho]_{w,m}$ is the spectrum-averaged mass energy absorption coefficient ratio water/medium. This relationship and its rationale agree with the proposal made by Reynaert et al. for bone.[27]

The CF for $D_{w,m}$ can be calculated using the relationship between $D_{w,m}$ and $D_{m,m}$, corresponding to stopping power ratios (small cavity of water surrounded by medium):[22,28]

$$CF_{m,D_{w,m}}^{beam} = \frac{D_{w,m*}}{D_{w,m}} = \left[\frac{\overline{\mu_{en}}}{\rho}\right]_{w,m}\left[\frac{\overline{S_{el}}}{\rho}\right]_{m,w} \quad \#(4)$$

where $[\overline{S_{el}}/\rho]_{m,w}$ is the spectrum-averaged mass collision stopping power ratio medium/water.

The calculation of the CFs using this theoretical approach is not trivial and can involve considerable uncertainties. To overcome this problem, we followed a more straightforward method

that yields the same values and uses solely dose distributions calculated within the algorithm. The in-depth details of the procedure can be found in a previous publication.[22] In summary, it involves two homogeneous virtual phantoms with the same density: one with the medium composition and another made of water. Both phantoms are irradiated identically with the considered beam, and the $D_{w,m}$ or $D_{m,m}$ distribution is calculated. Then, the CFs for each dose reporting mode *x* can be obtained from the ratio of doses along the central beam axis either at a reference depth *z* beyond both maximums $z_{max,m}$ and $z_{max,w}$, or at the depth of each maximum according to this expression:

$$CF_{m,Dx}^{beam} = \frac{D_{w,w}(z)/PDD_w(z)}{D_{x,m}(z)/PDD_m(z)} \cdot \frac{(SSD + z_{max,w})^2}{(SSD + z_{max,m})^2} = \frac{D_{w,w}(z_{max,w})}{D_{x,m}(z_{max,m})} \cdot \frac{(SSD + z_{max,w})^2}{(SSD + z_{max,m})^2} \#(5)$$

where $PDD_w(z)$ and $PDD_m(z)$ are the percentage depth doses at depth *z* for the water and medium phantom respectively, and SSD is the source to surface distance.

The CFs obtained using this simple method transform $D_{m,m}$ or $D_{w,m}$ into $D_{w,m*}$ distributions, as can be proved using equations 1 and 5 for a voxel at any position *s* beyond the build-up regions:

$$D_{w,m*}(s) = D_{x,m}(s) \cdot CF_{m,D_x}^{beam} =$$

$$= \frac{\int_0^{E_{max}} \Phi_{E,m}^{prim}(s) \left[\frac{S_{el}(E)}{\rho}\right]_x dE \cdot \int_0^{E_{max}} \Phi_{E,w}^{prim}(z_{max,w}) \left[\frac{S_{el}(E)}{\rho}\right]_w dE}{\int_0^{E_{max}} \Phi_{E,m}^{prim}(z_{max,m}) \left[\frac{S_{el}(E)}{\rho}\right]_x dE} \cdot \frac{(SSD + z_{max,w})^2}{(SSD + z_{max,m})^2} =$$

$$= \cdots = \int_0^{E_{max}} k_{w,m}(E) \cdot \Phi_{E,m}^{prim}(s) \left[\frac{S_{el}(E)}{\rho}\right]_w dE \#(6)$$

where $k_{w,m}(E) = \Phi_{E,w}^{prim}(z_{max,w}) / \Phi_{E,m}^{prim}(z_{max,w})$ is an energy-dependent factor characteristic of the medium. This fulfils $D_{ref,m*}$ requirements: dose is reported in a water voxel; the primary fluence in the voxel is that of radiation transport in medium; and $k_{w,m}(E)$ corrects the fluence by removing or adding the extra or missing primary electrons from a surrounding medium different from water.

There is internal consistency in the straightforward methodology because it only uses dose distributions calculated within the algorithm. This guarantees the same $D_{w,m*}$ distribution regardless of whether $D_{w,m}$ or $D_{m,m}$ are used as a starting point. The validity of the CFs may be compromised either in the build-up/build-down regions or near the interface between two different tissues since the assumptions made for deriving the CFs may not be fulfilled (δ-ray equilibrium and no charged particle

spectral changes with depth). The interface effect is limited to, at most, 2-3 millimeters and is smoothed out if 2 mm or greater voxels are used.[22,27] Regarding field size and penumbrae, no influence is expected since the charged particle spectrum is not modified.[29]

## 2.C. General workflow

Fig. 2 illustrates the workflow of the study. A realistic clinical scenario was used to optimize the dose to the PTV in different test cases for the four dose quantities. The plans for all quantities had the same optimization setup and objectives, and should ideally report the same final dose distribution.

For each case, a preliminary optimization was performed using the C/S algorithm of the optimizer, and the resulting plan was calculated for each dose quantity. Each dose distribution was then re-optimized to correct any deviation from the optimization objectives introduced by the algorithm/dose quantity and not considered by the internal algorithm in the previous optimization. Finally, we analyzed the dose distribution, photon energy fluence distribution (surrogate), robustness, and complexity of the plans. Each step of the process is described in the sections that follow.

## 2.D. Clinical scenario

We used a realistic clinical scenario to plan all the cases with volumetric modulated arc therapy (VMAT) for a 6 MV photon beam from a Varian TrueBeam accelerator (Varian Medical Systems) with a Millennium 120-leaf MLC.

The planning process was performed in the Eclipse v15.0.6 TPS (Varian Medical Systems, Palo Alto, CA, USA), using three of its algorithms:[30] the Analytical Anisotropic Algorithm (AAA), the Acuros XB (AXB) algorithm, and the Photon Optimizer (PO) algorithm. The AAA is a convolution-based algorithm with precomputed water deposition kernels that was used to obtain the $D_{w,w}$ distributions. The AXB algorithm is an advanced deterministic algorithm that explicitly solves the LBTE and yielded the $D_{m,m}$ and $D_{w,m}$ distributions. The $D_{ref,m*}$ distributions were derived from the corresponding AXB distributions using the methodology and the in-house software described later in

this section. The PO algorithm is used by the optimizer to determine the optimal field shape and intensity by iteratively conforming the dose distribution to the desired objectives.

The PO algorithm drives the optimization process.[30–32] In VMAT optimization, it generates a sequence of control points (178 in a full arc) that define MLC shapes and monitor units (MU) per degree as a function of gantry angle. All control points are used to optimize the plan, but they are grouped in sectors distributed evenly in each field. The angle resolution of the sectors goes through four levels, progressively increasing their number and the calculation accuracy. The fluence from each sector is optimized by minimizing an objective function that combines the dose-volume objectives. For a given objective *j*, the range of voxels *i* inside the structure that does not meet the goal gets assigned a penalty cost that is added to the total objective function:

$$cost_{j,i} = w_j \cdot \left(D_i - D_{goal\ j}\right)^2 \#(7)$$

where $w_j$ is the weight related with the priority defined for the objective, $D_i$ is the dose of the voxel *i* from the optimizer, and $D_{goal\ j}$ is the dose goal.

PO uses a simple C/S algorithm yielding $D_{w,w}$ for fast dose estimation in each iteration. It uses point spread kernels and accounts for heterogeneities by scaling water density and changing the dose distribution's slope as older pencil beam convolution algorithms. Therefore, when the optimized plan is calculated with a different algorithm, there can be discrepancies between the dose distribution considered within the optimization and the final dose distribution. PO accommodates the 'intermediate dose' option before proceeding with multi-resolution level three or four to reduce these discrepancies. It calculates a correction term by subtracting the optimizer dose matrix from the dose calculated with the final algorithm. This term is then added to the internal doses from subsequent iterations, turning equation 7 into:

$$cost_{j,i} = w_j \cdot \left(D_i + (D_{ID\ i} - D_{PO\ i}) - D_{goal\ j}\right)^2 \#(8)$$

where $D_{IDi}$ and $D_{POi}$ are the voxel *i* doses calculated with the intermediate dose and PO algorithms, respectively. By doing so, the cost function includes the discrepancies between both algorithms, and the fluences from the sectors are adjusted to compensate for such discrepancies. The intermediate dose

can be done automatically during the optimization or manually by performing a second optimization that uses the result of the previous one as input.

Regarding patient images and medium characterization, all CT scans were performed with a GE Optima CT580 W CT Scanner (GE Healthcare, Chicago, IL, USA). The TPS derives each CT voxel's medium characteristics from its CT number, but the process differs depending on the algorithm. AAA and PO require the voxel electron density, obtained using the CT number-to-electron density calibration curve for the scanning protocol. For AXB, the mass density and atomic composition of the voxel are needed. The mass density is determined by applying the user-defined CT number-to-density calibration curve for the scanning protocol, and is then linked to a material with a well-known composition specified in the AcurosXB-13.5 material library.[30] The library comprises air and five ICRP 1975 tissues for automatic assignment: lung, adipose tissue, muscle, cartilage, and bone. Each of these materials has an associated density range with overlapping regions between adjacent tissues to enable smooth transitions. This overlap is modeled to change linearly from one tissue to another, providing a mixture corresponding to the weighted proportion of materials. The library also includes 16 non-biological materials that users can assign manually.

In the present study, $D_{w,m*}$ distributions were derived from $D_{m,m}$ using the CFs given in Fig. 3 for the AXB tissues, the 6 MV photon beam used, and both dose reporting modes. These CFs were obtained with the straightforward procedure using equation 5.[22] They are independent of density for fixed material compositions and, in the overlapping regions, the linear mixture of nearby pure tissues results in a linear transition between CFs.

To that aim, we developed a Python program that converts $D_{m,m}$ or $D_{w,m}$ distributions to $D_{w,m*}$ distributions.[22] It takes the patient's CT images, RT structure, and RT dose DICOM files exported from the TPS and applies the corresponding CF to each dose voxel in a three-step process. Firstly, it mimics AXB media characterization to convert the CT image into a mass density matrix. Secondly, it transforms the mass density matrix into a CF matrix by using the density-to-CF table for the considered beam and dose reporting mode of the original dose distribution. Finally, it applies the CF matrix to the initial dose grid. Since image and dose voxels can differ in size and position, the software

used the average value of the CFs within the dose voxel (weighted by partial volumes). The final distributions were stored as RT dose DICOM files and subsequently imported into the TPS, enabling its evaluation with the TPS built-in tools and its use in the optimization process.

We used similar resolutions for the different grids involved to minimize partial volume effects and aliasing. We acquired CT images with 1.25 mm slice thickness, optimized using 1.25 mm resolution for PO structures and calculations, and computed the dose distributions with 1 mm voxel size.

## 2.E. Cases

The test cases included Sterpin's virtual case and several clinical cases that represent different situations in which composition or density heterogeneities are typically found inside the PTV in clinical practice. These heterogeneities are usually located outside the CTV (e.g. anatomical barriers like the skull or the mandible for brain or head and neck tumors), but can also be found within the CTV (e.g. fiducial markers, calcifications), or even constitute the target itself (e.g. lung or spinal treatments).

Unless otherwise specified, the prescription was done to PTV median dose and the goal was to irradiate the PTV uniformly.[33] The dose prescriptions, limits to the organs-at-risk (OAR), and VMAT arc configurations are specified in Table I. The cases are illustrated in the results (Figures 4-6) and described below:

(a) The virtual case studied by Sterpin to illustrate the impact on plan robustness against geometric errors of $D_{m,m}$ in PTV-based planning optimization.[18] It consisted of a cylindrical CTV made of water and measuring 7 cm in diameter, surrounded by a 1.2 cm CTV-PTV margin composed of bone. The PTV was embedded in a cylindrical water phantom with a 20 cm diameter.

(b) A complex head and neck case with heterogeneities outside the CTV, involving air, soft tissue, bone, teeth, and metal implants (titanium alloy assigned). Accelerated simultaneous boost was delivered to three target volumes. The PTV54, PTV60, and PTV70 encompassed the tumor plus nodal regions at risk, the tumor and high-risk nodal regions, and the tumor alone with a 5

mm margin. In addition to the OARs limits, $D_{2\%}$ for the mandible (metal implants excluded) and $D_{mean}$ for the oral cavity (surrogate for the oral mucosa) were also recorded.

(c) A peripheral lung tumor where accurate radiation transport was crucial owing to lateral charged particle disequilibrium. A 4DCT was used to delineate the tumor in each respiratory phase (10 bins). These volumes were combined to generate an internal target volume (ITV) with a diameter of 3.2 cm, and the PTV was obtained by adding a 5 mm margin. Planning was performed on the mid-ventilation CT. The dose prescription was done to PTV $D_{95\%}$, thus allowing higher doses within the PTV. It was planned with stereotactic body radiotherapy (SBRT), applying modulation restrictions through user-defined MU bounds to minimize the interplay effect.

Two more cases are presented in the Supplementary Material to show other clinical scenarios of interest. The first one is a peripheral brain tumor with the PTV including part of the cranial vault. It is conceptually similar to Sterpin's virtual case in that the tumor (CTV) is homogeneous but the PTV (CTV plus 5 mm) contains bone. The second one is a prostate (CTV) containing three fiducial markers. The fiducials were included in the CTV and the PTV was obtained by adding a 5 mm margin.

## 2.F. Plan optimization for each dose quantity

We used the same plan setup, optimization settings, objectives, and priorities for optimizing $D_{m,m}$, $D_{w,m}$, $D_{w,m^*}$, and AAA $D_{w,w}$ in each case. In this way, fair comparisons were ensured since any differences in the outcomes would be attributable to the specific characteristics of the quantities.

Ideally, the plans should have been optimized directly using each dose quantity for the corresponding dose calculations, but this was not possible in Eclipse because PO only uses a dedicated simple C/S algorithm. To overcome this limitation, we used the "intermediate dose" option described in Section 2.D. Firstly, a common preliminary optimization was performed and the dose distribution calculated for each quantity (without renormalization). These intermediate dose distributions could then be introduced into a second optimization as an intermediate dose before the initiation of multi-

resolution level three. The optimizer minimized the cost function (equation 8) by adjusting the fluences in the remaining levels to compensate the differences between PO's internal algorithm and the considered algorithm/dose quantity, resulting in distinct plans optimized for each quantity. The final plans were normalized according to the prescription.

## 2.G. Plan analysis

Plan quality is typically evaluated through the calculated dose distribution in a nominal scenario. However, uncertainties in the dose calculation and treatment delivery, and variations in patient setup and anatomy can affect the dose delivered to the patient and the resulting overall treatment quality.[34] Consequently, we evaluated the plan's dose distribution as well as its robustness to setup errors and its complexity. We also computed the energy fluence distribution in the patient to facilitate interpretation of the results.

The dose distributions were evaluated quantitatively using dose-volume-histograms (DVH) and the following DVH-based metrics:

(a) The ICRU 83 reporting parameters for the target volumes:[33] near-minimum dose $D_{98\%}$, median dose $D_{50\%}$, near-maximum dose $D_{2\%}$, and homogeneity index $HI=(D_{2\%}-D_{98\%})/D_{50\%}$. For Sterpin's case, the evaluation was performed in subvolumes located at the center of the phantom to avoid any edge effects at either end of the target. For the SBRT lung case, the conformity index CI and the gradient index GI, as defined in ICRU 91,[9] were also registered.

(b) The OAR constraint parameters listed in section 2.E.

We also visually assessed the dose distributions slice-by-slice to evaluate their spatial characteristics and investigate the spatial correlations between dose and tissue heterogeneities. We performed these evaluations with reference to detailed composition information for each structure, provided by the in-house software developed for obtaining $D_{w,m^*}$ distributions.

Plan robustness was studied against setup errors, which constitute the main uncertainties in MV photon treatments.[35] The additional treatment scenarios consisted of rigid translational setup errors (no

rotations) in both directions of the three cartesian axes and towards the nearest main heterogeneity (worst-case scenario). The isocenter of the plan was shifted the distance of the CTV-PTV margin, as the purpose of the PTV is to guarantee CTV coverage. Robustness was quantified by the variations in the above-mentioned CTV and OAR dosimetric parameters across the different scenarios.

Apart from robustness, plan complexity has also been considered because it may affect the uncertainty in dose calculation and delivery, and constitutes a relevant aspect in treatment verifications and plan quality assessment.[34,36] Plan complexity was evaluated by computing complexity indices that allow for a detailed analysis of the dynamic parameters involved in VMAT treatment plans. They were obtained using software developed by a working group of the Catalan Society of Medical Physicists (SCFM).[37] This software, written in MATLAB® (MathWorks, Inc.), calculates complexity indices using the data contained in the DICOM plan. All the beams in the plan were joined and calculations were performed for the "combined" beam. For this study, we evaluated the following complexity indices:

(a) Total number of MU.

(b) Small aperture score with 10 mm threshold (SAS10), defined as the fraction of open leaf pairs with an aperture smaller than 10 mm.[38]

(c) Modulation complexity score (MCS),[37] which integrates the variability in the shape of segments and variations in their area weighted by the MUs between control points. MCS values range from 0 to 1, and lower values indicate higher complexity (unlike the other indices).

To understand how the plans produce the different dose distributions, we assessed differences in photon energy fluence spatial distributions. Accurate computation of these fluence distributions requires MC calculations, but this is a complex process requiring external tools. Furthermore, accuracy is less important than the differences in fluence distributions between plans, and their spatial correlation with tissue heterogeneities. For this reason, all the final plans were re-calculated with the AAA algorithm, and these distributions were used as surrogates for fluence comparisons. While AAA is less accurate, its dose values are not sensitive to atomic composition heterogeneities, which means it can identify actual fluence differences without the interference of heterogeneity effects.

## 3. RESULTS

Fig. 4, 5, and 6 summarize the results for Sterpin's, head and neck, and lung cases. The details of the dose metrics, robustness, and complexities are presented in the sections that follow. The results for the brain and the prostate with fiducial markers cases are shown in the Supplementary Material.

The cases with involvement of both soft tissue and high-density heterogeneities followed the same pattern (Fig. 4 and 5). Compared with the other quantities, AXB $D_{m,m}$ reported lower dose values in the heterogeneities after the first optimization. This was offset in the second optimization by local fluence increases in order to achieve the planning objectives in the nominal scenario. However, these additional fluence modulations impacted negatively on plan robustness. Any positional mismatch between the high-fluence regions and the heterogeneities produced hot spots in the higher fluence locations while the heterogeneities became cold again. For AXB $D_{w,m}$, the pattern was similar but more pronounced and also inverse, with local fluence decreases to compensate for high dose values. In contrast, neither AXB $D_{w,m*}$ nor AAA $D_{w,w}$ presented dose inhomogeneities after the first optimization; hence there was no need for fluence adaptation and the resulting distributions were robust in the shifted scenarios.

In the lung SBRT case (Fig. 6), the PTV was composed almost exclusively of lung and there were no remarkable differences between AXB $D_{m,m}$, $D_{w,m}$, and $D_{w,m*}$. However, AAA $D_{w,w}$ differed from the other quantities, as can be seen in the first calculation and the fluence distribution.

The visual inspection of the fluence distributions showed that all AXB $D_{m,m}$ and AXB $D_{w,m}$ fluence fluctuations corresponded to the composition heterogeneity regions where cold and hot spots appeared in the first calculation. In the head and neck case in which the PTV comprised mainly muscle, the AXB $D_{m,m}$ fluences were always 1% higher than the rest.

When the PTV contained different media, most dose inhomogeneities introduced by AXB $D_{m,m}$ and AXB $D_{w,m}$ were corrected in the second optimization, but some small dose variations remained around material interfaces. This can be seen in Sterpin's case as a narrow ring between the CTV and the PTV (hot for AXB $D_{m,m}$, cold for AXB $D_{w,m}$), and in the head and neck case around the implant, the teeth and the air gap between them. In Sterpin's case, these small dose inhomogeneities had a slight impact

on CTV robustness (see DVHs in Fig. 4). In the head and neck case, dose variations were imperceptible in the DVHs owing to the smaller relative size of the medium heterogeneities. The variations were mainly attributable to the distance required for fluence values to transition from the background level to the level required for offsetting dose inhomogeneities. For $D_{w,m*}$ there were also some minor dose fluctuations at material interfaces caused by partial volume effects between image and dose grids, and by the uncertainty at material interfaces of the CFs used for deriving the quantity.

## 3.A. Dose distributions in the nominal scenario

PTV and OAR tissue compositions and dosimetric parameters in the nominal scenario are presented in Fig. 7. This information is also provided in numerical form in Supplementary Material Tables SMI and SMII. The parameters adopted for plan normalization ($D_{50\%}$ for Sterpin and head and neck cases; $D_{95\%}$ for lung SBRT) are not shown as they were forced to equal the prescription dose for all quantities in the final calculations.

Where 2% or more of the PTV consisted of a material with a different dose response, minimum ($D_{98\%}$) and maximum ($D_{2\%}$) PTV doses were compromised for AXB $D_{m,m}$ and AXB $D_{w,m}$, respectively. In Sterpin's and head and neck cases, where the bone component exceeded 2% of the PTV, $D_{98\%}$ was below 95% of the prescribed dose after the first optimization for AXB $D_{m,m}$, and $D_{2\%}$ was above 105% for AXB $D_{w,m}$. These divergences were reflected in worse HIs. In the head and neck case, where the PTV contained 2% metal, even greater differences were observed. In the second optimization, all metrics were forced to converge and there were no notable differences between the dose quantities, although the results were slightly better for AAA $D_{w,w}$ and AXB $D_{w,m*}$, followed by AXB $D_{m,m}$, and finally AXB $D_{w,m}$.

In the lung case, the PTV was composed almost exclusively of lung tissue. All the quantities obtained from AXB behaved similarly, with almost identical values in both optimization steps. In contrast, AAA $D_{w,w}$ exhibited higher $D_{98\%}$ in the first calculation and, despite converging with the other quantities at the end of the process, presented different doses outside the target (lower GI).

Regarding the OARs, after the first common optimization, we observed higher AXB $D_{w,m}$ and lower AXB $D_{m,m}$ for the organs of the head and neck case with bony composition (cochleae and mandible), while AAA $D_{w,w}$ differed in the larynx (lung content) and the parotid glands (near the surface). The differences between the first and the second optimization were due to the changes in the incident photon fluence geometry required for PTV optimization. For the parotid glands of the head and neck case, these changes increased $D_{mean}$ and it was forced to be kept within its limit for each quantity. For the mandible, AXB $D_{w,m}$ maximums were reduced because they were located inside the PTV and the optimization kept $D_{2\%}$ below 70 Gy. Finally, in the lung case, V20Gy for both lungs minus the CTV was lower for AAA $D_{w,w}$.

## 3.B. Robustness to setup errors

The variations of the CTV dosimetric parameters across the shifted scenarios after both optimizations are presented in Table II. Variations affecting the OARs were within 2% in all cases.

In the lung SBRT case, there were no tissues with different dose responses. Although there were variations in the parameters due to the high dose gradient, these variations were similar across the quantities and all of them were equally robust (paired differences in each optimization within 2%).

In the other cases, robustness depended on the dose quantity. The first optimization, based on the PO's C/S algorithm, was always robust (all parameters differed from the nominal scenario by less than 2%). The second optimization was also robust for AXB $D_{w,m*}$ and AAA $D_{w,w}$, but not for AXB $D_{m,m}$ and AXB $D_{w,m}$.

Hot regions appeared for AXB $D_{m,m}$ (Figures 4 and 5), with $D_{2\%}$ around 3% higher than the nominal scenario if bone was present and almost 7% higher if there was metal.

We observed the opposite pattern and more extreme differences for AXB $D_{w,m}$, where the second optimization produced cold regions that mainly affected $D_{98\%}$. Differences from the nominal scenario were around -7% for bone and -17% for metal. In the head and neck case, these larger AXB $D_{w,m}$

responses, combined with the size of heterogeneities relative to the CTV, also influenced $D_{50\%}$ and $D_{2\%}$ (around -3% and +3% respectively).

Assessing the scenarios slice by slice, we found that this lack of robustness for AXB $D_{m,m}$ and AXB $D_{w,m}$ was due to positional mismatches between atomic composition heterogeneities and the corresponding fluence compensations introduced in the second optimization.

## 3.C. Complexity

Fig. 8 presents the complexity index values obtained in the study. We found no major differences between the dose quantities in this regard.

For the lung case, the three quantities derived from AXB behaved similarly, while AAA $D_{w,w}$ was more complex in MU/Gy and MCS. In the other cases, AXB $D_{m,m}$ was between 3% and 10% more complex than AXB $D_{w,m*}$ in terms of MU/Gy. The differences in SAS10 and MCS varied with each case, though complexity was generally lower for AXB $D_{w,m*}$ and AXB $D_{w,m}$, and higher for AXB $D_{m,m}$. AAA $D_{w,w}$ laid somewhere in between.

# 4. DISCUSSION

For simplicity, in this section we will refer to the dose quantities without specifying the particular algorithm. Although the numerical results may vary for other algorithms (especially for C/S), the behavior and its impact should, in principle, be the same across algorithms of the same type.

Optimization using Eclipse's intermediate dose option produced similar dose distributions for all the dose quantities considered. The few notable differences, all within the optimization objectives, were caused by bony OARs in the head and neck case. However, the processes leading to these similar distributions differed, and this divergence could translate into varying doses delivered to patients.

On the one hand, using advanced algorithms reporting $D_{m,m}$ or $D_{w,m}$ can compromise robustness, modify the dose delivered to some atomic composition heterogeneities because of fluence corrections

and, to a lesser extent, increase complexity. On the other hand, C/S algorithms may not achieve the required accuracy in some cases. $D_{ref,m*}$ overcomes the issues associated with the other three dose quantities.

## 4.A. Use of advanced algorithms reporting $D_{m,m}$ or $D_{w,m}$

Sterpin warned about the potential loss of robustness against setup errors when using $D_{m,m}$ in PTV-based plan optimization,[18] illustrating this effect using a virtual phantom with extreme cortical bone heterogeneity. Our study replicated and confirmed Sterpin's results and included other materials, other dose quantities, and representative clinical cases. In addition, we analyzed the resulting dose distributions and complexities in order to comprehensively assess plan quality.[34]

In the lung case, the differences between the optimizer's simple C/S algorithm and the advanced algorithm are due to radiation transport. The intermediate dose option penalizes these discrepancies, and the fluences are adjusted to minimize the cost function.

In the other cases, the shortcomings of $D_{m,m}$ and $D_{w,m}$ in terms of plan robustness are due to their different dose response in some atomic composition heterogeneities. The optimizer's algorithm has a flat dose response ($D_{w,w}$). Consequently, the penalty introduced in the intermediate dose requires local changes in the photon fluence distribution to compensate for the different dose values in the heterogeneities and fulfill the optimization goals. The effects of these changes are less pronounced for $D_{m,m}$ since the dose inhomogeneities are systematically lower and the dose distributions are smoother than for $D_{w,m}$, as expected from the behavior of both quantities.[12,13]

It is worth noting that the optimization objectives are designed for previous algorithms yielding $D_{w,w}$, and the fluence adjustments result from attempting to mimic the homogeneity characteristics of $D_{w,w}$ distributions. This approach can be inherently unrobust and involve clinical inconsistencies.

Reduced plan robustness applies to $D_{m,m}$ and $D_{w,m}$ because dose distributions are impaired if there is any positional mismatch between the fluence adjustments and the heterogeneities they compensate for. This results in a violation of the static dose cloud approximation, i.e. the assumption that the dose

distribution in treatment room coordinates is unaffected by changes in patient geometry.[35] In a shifted scenario, the local fluence inhomogeneity will affect adjacent tissues different from those initially intended in the nominal scenario, while the dose delivered to the heterogeneity returns to its initial value in the absence of the fluence compensation. This effect is more pronounced in Sterpin's virtual case than in real patients, where the mixture of materials is smoother and the composition less extreme. It is remarkable nonetheless, with hotter regions between +3% (bone) and +7% (metal) affecting at least 2% of the CTV for $D_{m,m}$, and colder regions between -7% and -17% in the same materials for $D_{w,m}$.

An important aspect of reduced robustness is that it systematically affects regions adjacent to medium heterogeneities. This spatial correlation is not reflected in the DVHs and must be checked visually or by using texture analysis or doseomics.[34] This should be borne in mind when using automatic planning tools, as corrections can be made systematically and the reduction in robustness may be overlooked.

The implications of the loss in robustness depend on the tissues found in the shifted location and on the quantity used ($D_{m,m}$ or $D_{w,m}$). The hot regions that appear for $D_{m,m}$ in the shifted scenarios could improve tumor control probability (TCP) if they lie within the CTV, but may increase normal tissue complication probability (NTCP) if they are in nearby healthy tissue. The opposite occurs for $D_{w,m}$, with cold regions that can decrease either TCP or NTCP depending on whether the diminished fluence is moved towards the CTV or the healthy tissue.

From a clinical perspective, although final calculated dose distributions were apparently similar to those from $D_{w,w}$ because the optimizations were forced to yield the same results, the different fluences imply that patients actually receive different doses (see fluence distributions for Sterpin and head and neck cases in Figures 4 and 5). Besides, these adjustments occur in opposite directions for $D_{m,m}$ and $D_{w,m}$. Compared with previous algorithms, this results in higher delivered doses if $D_{m,m}$ is used and lower doses if $D_{w,m}$. Finally, when comparing results with reference clinical data, care should also be taken as this data is mainly based on dose distributions from algorithms without these effects.[17]

The choice of dose quantity has a modest impact on plan complexity, although it unequivocally affects some plan characteristics. For $D_{m,m}$, the MLC needs to shape to high density heterogeneities and increase the delivered fluence to those regions, as occurs with simultaneous integrated boosts. This increases complexity (higher SAS10 and lower MCS) and, in combination with the lower dose to muscle than dose to water values (1%), also increases MU/Gy. For $D_{w,m}$, on the other hand, the MLC needs to shield the heterogeneities to cool them but acts differently depending on their shape and size. For relatively small heterogeneities (head and neck) fewer leaves are used, and as a result SAS10 and MCS are unaffected. The situation is different for the Sterpin and the lung cases, with no notable differences in SAS10 or MCS between quantities. In Sterpin's case, this is attributable to the large heterogeneity size (no effect on MLC apertures below 10 mm) and regular shape. In the lung case, plan complexity was restricted in the optimization process and no large differences were found. It is important to note that these complexity results were obtained using Eclipse TPS. Other planning systems could use different strategies to achieve the necessary beam modulation, weighing the degrees of freedom differently (MLC, dose rate, gantry speed).[37]

## 4.B. Use of C/S algorithms reporting $D_{w,w}$

In this case, the type of algorithm and the dose quantity are the same as in the optimizer. $D_{w,w}$ values yielded by C/S algorithms under CPE conditions are not sensitive to atomic composition heterogeneities (Fano's theorem), meaning no extra compensations are required apart from eventual radiation transport discrepancies between both algorithms. As a result, photon fluence is more uniform, robustness remains stable, and the dosimetric parameters are slightly better. Nevertheless, C/S algorithms can fail when accurate radiation transport is crucial, as reported in the literature[9–11] and illustrated in the lung SBRT case, where the required fluence, gradient index, and MUs diverged from those of the other quantities, as would the dose delivered to the patient.

## 4.C. Use of advanced algorithms reporting $D_{ref,m*}$

The $D_{ref,m*}$ distributions are similar to those of $D_{m,m}$ and $D_{w,m}$, but switching off their different dose response in atomic composition heterogeneities. This offers several advantages in plan optimization and evaluation:

- Radiation transport accuracy. It is yielded by an advanced algorithm and the optimization is performed with the highest transport accuracy (unlike $D_{w,w}$).
- Evaluation of the dose distribution without heterogeneity distortions.
- Direct applicability of the evaluation parameters designed for C/S algorithms.[9,33]
- Production of more robust plans without increased complexity. The resulting plans are consistently robust because dose values remain stable regardless of medium heterogeneities and unrobust fluence compensations are therefore avoided. This behavior preserves the static dose cloud approximation further than $D_{m,m}$ or $D_{w,m}$, that is, the assumption that the CTV receives the prescribed dose as long as it stays within the PTV.[35]

Only $D_{ref,m*}$ fulfills these characteristics simultaneously, making it consistent and reliable in all situations. For users of C/S algorithms, adopting $D_{ref,m*}$ could facilitate the transition to advanced algorithms as it behaves similarly to $D_{w,w}$. For users of advanced algorithms, adopting $D_{ref,m*}$ could be useful in the planning process.

Using $D_{ref,m*}$ for optimization facilitates obtaining well-optimized, accurate, and robust plans. When there are no tissues with different dose responses, as in the lung case, it matches with $D_{m,m}$ and $D_{w,m}$ and is optimized equally. In the other cases, with atomic composition heterogeneities, its flat behavior in these regions is similar to the optimizer's algorithm (as seen in the DVHs after the first optimization in Figures 4 and 5). Consequently, the penalty term introduced by the intermediate dose option is almost zero, and no fluence adjustments are needed (as with $D_{w,w}$). The dose distributions are achieved more naturally since there are practically no effects to consider other than the optimization goals. Compared to $D_{m,m}$ and $D_{w,m}$, this is reflected in generally lower complexities, more uniform photon fluence distributions, slightly better dosimetric parameters and, above all, superior robustness.

$D_{ref,m*}$ properties also aid the decision-making process during plan optimization and the case discussions with radiation oncologists. It facilitates manual planning as no other strategies are needed, and could be particularly helpful in automatic planning, where there is no direct supervision and all the effects presented by the other quantities would otherwise have to be managed within the model.

Final dose reporting can be kept with $D_{m,m}$ or $D_{w,m}$, regardless of dose inhomogeneities, because $D_{ref,m*}$ is not related to any radiobiological consideration. $D_{ref,m*}$ aids to connect with the clinical data collected through previous algorithms, but calculations are moving towards advanced algorithms and it is one of their dose quantities that should be used to correlate with clinical outcomes. By adopting $D_{ref,m*}$ we can determine whether any failure by $D_{m,m}$ or $D_{w,m}$ distributions to fulfill treatment objectives is due to distortions caused by tissue heterogeneities. Furthermore, with this quantity we avoid the contradictory decisions that could be taken depending on whether $D_{m,m}$ or $D_{w,m}$ is used, thus improving consistency.

The reference medium chosen to report $D_{ref,m*}$ should be linked to the final dose reporting quantity, which must be consistent with the reference clinical data used in dose prescription. This means choosing muscle when reporting with $D_{m,m}$[15] (e.g. recent NRG/RTOG trials[14], consensus from the Global Harmonisation Group for clinical trials[17]), and water when reporting with $D_{w,m}$ or $D_{w,w}$ (e.g. older trials and studies, ICRU 91,[9] QUANTEC[39]). Nevertheless, the choice of reference medium does not notably affect the results; the difference between selecting water or muscle is a systematic factor of 0.99, corresponding to the ratio of water/muscle doses.[15] Since the factor is applied to the whole $D_{ref,m*}$ distribution, it only introduces an overall 1% shift in the dose distribution.

$D_{ref,m*}$ could be easily implemented as a built-in feature of the TPS. The CFs could be derived internally by the system during algorithm configuration, and doses could be reported directly as $D_{ref,m*}$ when necessary, with almost no time penalty. Thus, $D_{ref,m*}$-based optimization could be easily performed, either by automatically introducing it in an intermediate step (as shown for the Eclipse TPS) or applying it directly if the TPS uses an advanced algorithm for optimization.

## 5. CONCLUSIONS

Dose distribution can be optimized for all the dose quantities considered, achieving similar results. However, there are substantial differences in how the plans produce the distributions that can translate into differences in the doses delivered to patients.

Using $D_{w,w}$ from C/S algorithms may not be accurate enough when radiation transport accuracy is crucial. Advanced algorithms improve radiation transport accuracy, but dose distributions in terms of $D_{m,m}$ or $D_{w,m}$ can present pitfalls when used for plan optimization. The reason is their different dose response to some atomic composition heterogeneities, which are compensated in the optimization process by introducing local fluence modifications that can significantly depart from the static dose cloud approximation, thus decreasing robustness, and, to a lesser extent, increasing plan complexity.

$D_{ref,m*}$, which was recently introduced for advanced algorithms, has many of the strengths of the other quantities while avoiding their weaknesses. The advantages of radiation transport in medium are preserved, while dose values remain stable irrespective of heterogeneities, thus avoiding the dose distortions produced by $D_{m,m}$ and $D_{w,m}$ and their fluence compensations. The use of $D_{ref,m*}$ in plan optimization extends the validity of the static dose cloud approximation, resulting in accurate and robust plans without increasing complexity. Plan evaluation in terms of $D_{ref,m*}$ can be performed directly without the confounding factors of the other dose quantities, simplifying the treatment planning process. The implementation of $D_{ref,m*}$ in the TPS would be straightforward. This would avoid the need for more complex strategies and facilitate both manual and automatic planning, where there is no direct supervision and these situations should otherwise be managed within the model. The reporting of the final dose distribution can be kept with $D_{m,m}$ or $D_{w,m}$ to correlate with clinical outcomes.

In summary, the dose quantity used in MV photon optimization can affect plan robustness. Using $D_{ref,m*}$ offers advantages in both plan optimization and evaluation and can be easily implemented as a built-in feature of the TPS. This dose quantity improves the robustness of the treatment plans, produces more consistent results in all situations, and can facilitate the treatment planning process when using advanced dose calculation algorithms.

## DATA AVAILABILITY STATEMENT

The data that support the findings of this study are available from the corresponding author upon reasonable request.

## REFERENCES


1. ICRU. *ICRU Report 24: Determination of Absorbed Dose in a Patient Irradiated by Beams of X or Gamma Rays in Radiotherapy Procedures*.; 1976. doi:10.2214/ajr.118.4.938
2. IAEA. *Commissioning and Quality Assurance of Computerized Planning Systems for Radiation Treatment of Cancer, Technical Reports Series No 430*.; 2004.
3. Papanikolaou N, Battista J, Boyer A, et al. Tissue inhomogeneity corrections for megavoltage photon beams. AAPM Report No. 85, Task Group No 65 of the Radiation Therapy Committee of the American Association of Physicists in Medicine. Published online January 1, 2004.
4. *Accuracy Requirements and Uncertainties in Radiotherapy*. International Atomic Energy Agency; 2016. https://www.iaea.org/publications/10668/accuracy-requirements-and-uncertainties-in-radiotherapy
5. Knöös T, Wieslander E, Cozzi L, et al. Comparison of dose calculation algorithms for treatment planning in external photon beam therapy for clinical situations. *Phys Med Biol*. 2006;51(22):5785-5807. doi:10.1088/0031-9155/51/22/005
6. Papanikolaou N, Stathakis S. Dose-calculation algorithms in the context of inhomogeneity corrections for high energy photon beams. *Med Phys*. 2009;36(10):4765-4775. doi:10.1118/1.3213523
7. Chetty IJ, Curran B, Cygler JE, et al. Report of the AAPM Task Group No. 105: Issues associated with clinical implementation of Monte Carlo-based photon and electron external beam treatment planning. *Med Phys*. 2007;34(12):4818-4853. doi:10.1118/1.2795842
8. Bedford JL. Calculation of absorbed dose in radiotherapy by solution of the linear Boltzmann transport equations. *Phys Med Biol*. 2019;64(2):02TR01. doi:10.1088/1361-6560/aaf0e2
9. ICRU. *ICRU Report 91, Prescribing, Recording, and Reporting of Stereotactic Treatments with Small Photon Beams*.; 2017. doi:10.1007/s00066-018-1416-x
10. Miften M, Mihailidis D, Kry SF, et al. Management of radiotherapy patients with implanted cardiac pacemakers and defibrillators: A Report of the AAPM TG-203†. *Med Phys*. Published online December

1, 2019. doi:10.1002/mp.13838

11. Reft C, Alecu R, Das IJ, et al. Dosimetric considerations for patients with HIP prostheses undergoing pelvic irradiation. Report of the AAPM Radiation Therapy Committee Task Group 63. *Med Phys*. 2003;30(6):1162-1182. doi:10.1118/1.1565113
12. Andreo P. Dose to 'water-like' media or dose to tissue in MV photons radiotherapy treatment planning: still a matter of debate. *Phys Med Biol*. 2015;60(1):309-337. doi:10.1088/0031-9155/60/1/309
13. Ma C-M, Li J. Dose specification for radiation therapy: dose to water or dose to medium? *Phys Med Biol*. 2011;56(10):3073-3089. doi:10.1088/0031-9155/56/10/012
14. Gladstone DJ, Kry SF, Xiao Y, Chetty IJ. Dose Specification for NRG Radiation Therapy Trials. *Int J Radiat Oncol Biol Phys*. 2016;95(5):1344-1345. doi:10.1016/j.ijrobp.2016.03.044
15. Kry SF, Feygelman V, Balter P, et al. AAPM Task Group 329: Reference dose specification for dose calculations: dose-to-water or dose-to-muscle? *Med Phys*. Published online December 28, 2019:mp.13995. doi:10.1002/mp.13995
16. Al-Hallaq HA, Chmura SJ, Salama JK, et al. Benchmark Credentialing Results for NRG-BR001: The First National Cancer Institute-Sponsored Trial of Stereotactic Body Radiation Therapy for Multiple Metastases. *Int J Radiat Oncol Biol Phys*. 2017;97(1):155-163. doi:10.1016/j.ijrobp.2016.09.030
17. Kry SF, Lye J, Clark CH, et al. Report dose-to-medium in clinical trials where available; a consensus from the global Harmonisation group to maximize consistency. *Radiother Oncol*. 2021;159:106-111. doi:10.1016/j.radonc.2021.03.006
18. Sterpin E. Potential pitfalls of the PTV concept in dose-to-medium planning optimization. *Phys Med*. 2016;32(9):1103-1110. doi:10.1016/j.ejmp.2016.08.009
19. Andreo P, Burns DT, Nahum AE, Seuntjens JP, Attix FH. *Fundamentals of Ionizing Radiation Dosimetry*. WILEY-VCH; 2017.
20. Bouchard H, Seuntjens J, Duane S, Kamio Y, Palmans H. Detector dose response in megavoltage small photon beams. I. Theoretical concepts. *Med Phys*. 2015;42(10):6033-6047. doi:10.1118/1.4930053
21. Akdeniz Y, Yegingil I, Yegingil Z. Effects of metal implants and a metal artifact reduction tool on calculation accuracy of AAA and Acuros XB algorithms in small fields. *Med Phys*. Published online September 26, 2019:mp.13819. doi:10.1002/mp.13819
22. Jurado-Bruggeman D, Munoz-Montplet C, Vilanova JC. A new dose quantity for evaluation and optimisation of MV photon dose distributions when using advanced algorithms: proof of concept and

potential applications. *Phys Med Biol*. 2020;65(23):235020. doi:10.1088/1361-6560/abb6bc

23. Seltzer SM, Bartlett DT, Burns DT, et al. *ICRU Report 85: Fundamental Quantities and Units for Ionizing Radiation*. Vol 11.; 2011. doi:10.1093/jicru/ndr011
24. Ahnesjö A. Collapsed cone convolution of radiant energy for photon dose calculation in heterogeneous media. *Med Phys*. 1988;16(4):577-592.
25. Younes T, Chauvin M, Delbaere A, et al. Towards the standardization of the absorbed dose report mode in high energy photon beams. *Phys Med Biol*. 2021;66(4):045009. doi:10.1088/1361-6560/abd22c
26. Walters BRB, Kramer R, Kawrakow I. Dose to medium versus dose to water as an estimator of dose to sensitive skeletal tissue. *Phys Med Biol*. 2010;55(16):4535-4546. doi:10.1088/0031-9155/55/16/S08
27. Reynaert N, Crop F, Sterpin E, Kawrakow I, Palmans H. On the conversion of dose to bone to dose to water in radiotherapy treatment planning systems. *Phys Imaging Radiat Oncol*. 2018;5:26-30. doi:10.1016/j.phro.2018.01.004
28. Siebers J V., Keall PJ, Nahum AE, Mohan R. Converting absorbed dose to medium to absorbed dose to water for Monte Carlo based photon beam dose calculations. *Phys Med Biol*. 2000;45(4):983-995. doi:10.1088/0031-9155/45/4/313
29. IAEA. *Dosimetry of Small Static Fields Used in External Beam Radiotherapy, Technical Reports Series No. 483*.; 2017. Accessed April 5, 2020. https://www.iaea.org/publications/11075/dosimetry-of-small-static-fields-used-in-external-beam-radiotherapy
30. Varian Medical Systems. *Eclipse Photon and Electron Algorithms Reference Guide*.; 2017.
31. Vanetti E, Nicolini G, Nord J, et al. On the role of the optimization algorithm of RapidArc® volumetric modulated arc therapy on plan quality and efficiency. *Med Phys*. 2011;38(11):5844-5856. doi:10.1118/1.3641866
32. Li Y, Rodrigues A, Li T, Yuan L, Yin FF, Wu QJ. Impact of dose calculation accuracy during optimization on lung IMRT plan quality. *J Appl Clin Med Phys*. 2015;16(1):219-228. doi:10.1120/jacmp.v16i1.5137
33. ICRU. *ICRU Report 83: Prescribing, Recording, and Reporting Intensity-Modulated Photon-Beam Therapy (IMRT)*.; 2010. doi:10.1093/jicru/10.1.Report83
34. Hernandez V, Hansen CR, Widesott L, et al. What is plan quality in radiotherapy? The importance of evaluating dose metrics, complexity, and robustness of treatment plans. *Radiother Oncol*. 2020;153:26-33. doi:10.1016/j.radonc.2020.09.038

35. Unkelbach J, Alber M, Bangert M, et al. Robust radiotherapy planning. *Phys Med Biol*. 2018;63(22). doi:10.1088/1361-6560/aae659

36. Miften M, Olch A, Mihailidis D, et al. Tolerance limits and methodologies for IMRT measurement-based verification QA: Recommendations of AAPM Task Group No. 218. *Med Phys*. 2018;45(4):e53-e83. doi:10.1002/mp.12810

37. Hernandez V, Saez J, Pasler M, Jurado-Bruggeman D, Jornet N. Comparison of complexity metrics for multi-institutional evaluations of treatment plans in radiotherapy. *Phys Imaging Radiat Oncol*. 2018;5:37-43. doi:10.1016/j.phro.2018.02.002

38. Crowe SB, Kairn T, Kenny J, et al. Treatment plan complexity metrics for predicting IMRT pre-treatment quality assurance results. *Australas Phys Eng Sci Med*. 2014;37(3):475-482. doi:10.1007/s13246-014-0274-9

39. Bentzen SM, Constine LS, Deasy JO, et al. Quantitative Analyses of Normal Tissue Effects in the Clinic (QUANTEC): An Introduction to the Scientific Issues. *Int J Radiat Oncol Biol Phys*. 2010;76(3 SUPPL.). doi:10.1016/j.ijrobp.2009.09.040

## CONFLICT OF INTEREST

The authors have no conflicts of interest to declare.

## FIGURE LEGENDS

FIG. 1. Illustration of the different dose concepts in bone (watery cells within structures with different densities and compositions). Photon radiation transport to the voxel (black waves) can be calculated through water or media of different densities. Energy deposition in the voxel depends on voxel's composition and the electron fluence generated in the surrounding medium (red tracks). Different combinations of the media involved result in different dose quantities. $D_{w,w}$: transport in water and dose deposition in water surrounded by water. $D_{w,m}$: transport in media and dose deposition in water surrounded by medium. $D_{m,m}$: transport in media and dose deposition in medium surrounded by medium. $D_{ref,m*}$: transport in media and, for water as reference medium, dose deposition in water surrounded by water-like medium.

FIG. 2. Global workflow of the study. A set of representative cases (sketch shown as example) was optimized in the PTV for $D_{m,m}$, $D_{w,m}$, $D_{ref,m*}$, and $D_{w,w}$ (C/S) using the same optimization setup and conditions, ending up with a similar final dose distribution for each dose quantity. Step 1: first optimization using the convolution/superposition algorithm of the optimizer. Step 2: the resulting optimized plan was then calculated for each dose quantity. Step 3: these dose distributions were re-optimized to correct any deviations from the optimization goals introduced by the algorithm/dose quantity. Step 4: analysis and comparison of the dose distributions, energy fluence distributions (surrogate), robustness, and complexities.

FIG. 3. (a) Dose correction factors (CFs) for 6 MV photons for each mass density in AXB when automatic material assignment is used: $CF^{6MV}_{mAXB,Dmm}$ (red) and $CF^{6MV}_{mAXB,Dwm}$ (blue). The points correspond to the determined CFs, and the lines are linear interpolations between consecutive points. The tissues assigned at each density are presented at the bottom. In the regions with overlapping tissues, the proportion of each tissue in the mixture is shown by the boundary between them. (b) The CF values for the AXB biological tissues and titanium alloy.

FIG. 4. Sterpin's case. The rows summarize the results for AXB $D_{m,m}$ (red), AXB $D_{w,m}$ (blue), AXB $D_{w,m*}$ (green), and AAA $D_{w,w}$ (yellow). The columns summarize each part of the study: first and second optimizations, photon fluence distribution (surrogated by AAA calculations), and robustness. The dose distributions are shown in a representative slice (orange and red contours for CTV and PTV, respectively); worst-case scenario for robustness. DVHs for the PTV are presented at the bottom of the first three columns. The robustness column includes a CTV DVH for each quantity in the nominal (solid) and shifted (dashed) scenarios. CTV and PTV mass density differential histograms are shown in the lower-right corner.

FIG. 5. Head and neck case. The rows summarize the results for AXB $D_{m,m}$ (red), AXB $D_{w,m}$ (blue), AXB $D_{w,m*}$ (green), and AAA $D_{w,w}$ (yellow). The columns summarize each part of the study: first and second optimizations, photon fluence distribution (surrogated by AAA calculations), and robustness. The dose distributions are shown in a representative slice (orange and red contours for CTV and PTV, respectively); worst-case scenario for robustness. DVHs for the PTV are presented at the bottom of the first three columns. The robustness column includes a CTV DVH for each quantity in the nominal (solid) and shifted (dashed) scenarios. CTV and PTV mass density differential histograms are shown in the lower-right corner.

FIG. 6. Lung SBRT case. The rows summarize the results for AXB $D_{m,m}$ (red), AXB $D_{w,m}$ (blue), AXB $D_{w,m*}$ (green), and AAA $D_{w,w}$ (yellow). The columns summarize each part of the study: first and second optimizations, photon fluence distribution (surrogated by AAA calculations), and robustness. The dose distributions are shown in a representative slice (orange and red contours for CTV and PTV, respectively); worst-case scenario for robustness. DVHs for the PTV are presented at the bottom of the first three columns. The robustness column includes a CTV DVH for each quantity in the nominal (solid) and shifted (dashed) scenarios. CTV and PTV mass density differential histograms are shown in the lower-right corner.

FIG. 7. PTVs (a) and OARs (b) tissue composition and dosimetric parameters in the nominal scenario. The composition chart shows the percentage of each pure tissue within the volume (densities in the overlapping regions are decomposed into their pure components). The hollow circles mark the values of the dosimetric parameters for AXB $D_{m,m}$ (red), AXB $D_{w,m}$ (blue), AXB $D_{w,m*}$ (green), and AAA $D_{w,w}$ (yellow) after the second optimization. For the PTVs, the first calculation results are also shown (filled circles). For the OARs, a red line indicates the limit established for the parameter. $D_{X\%}$ corresponds to the dose covering X% of the volume; $D_{mean}$ is the volume mean dose; $V_{XGy}$ represents the volume receiving at least X Gy; and HI, CI, and GI are the homogeneity, conformity, and gradient indices, respectively.

FIG. 8. MUs per prescribed Gy, small aperture score with 10 mm threshold (SAS10), and modulation complexity score (MCS) for AXB $D_{m,m}$ (red), AXB $D_{w,m}$ (blue), AXB $D_{w,m*}$ (green), and AAA $D_{w,w}$ (yellow) in each case. MU/Gy values are presented relative to the AXB $D_{w,m*}$ values. Higher MU/Gy, higher SAS10, and lower MCS indicate higher complexity.

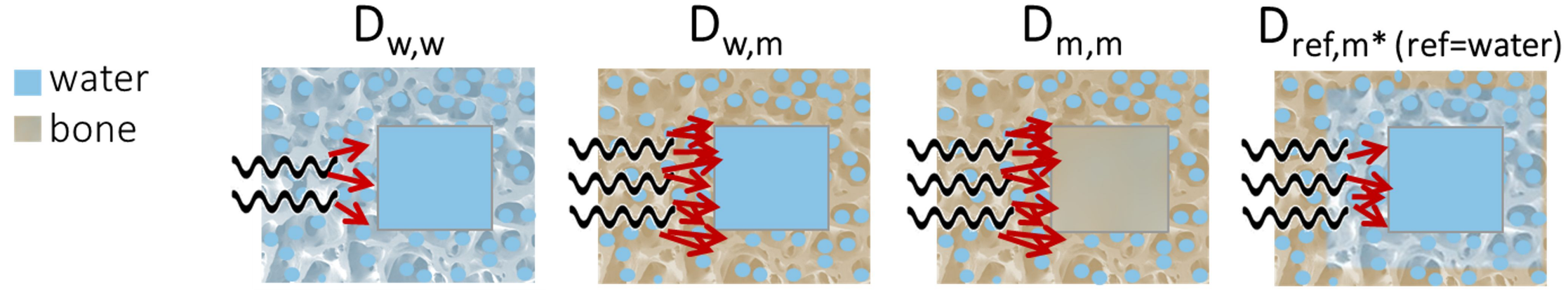


| | $D_{w,w}$ | $D_{w,m}$ | $D_{m,m}$ | $D_{ref,m}$* (ref=water) |
|---|---|---|---|---|
| Radiation transport in | water | media | media | media |
| Surrounding medium | water | bone | bone | “water” |
| Voxel | water | water | bone | water |
| Dose value vs $D_{w,w}$ | - | ↑↑ | ↓ | ≈ |

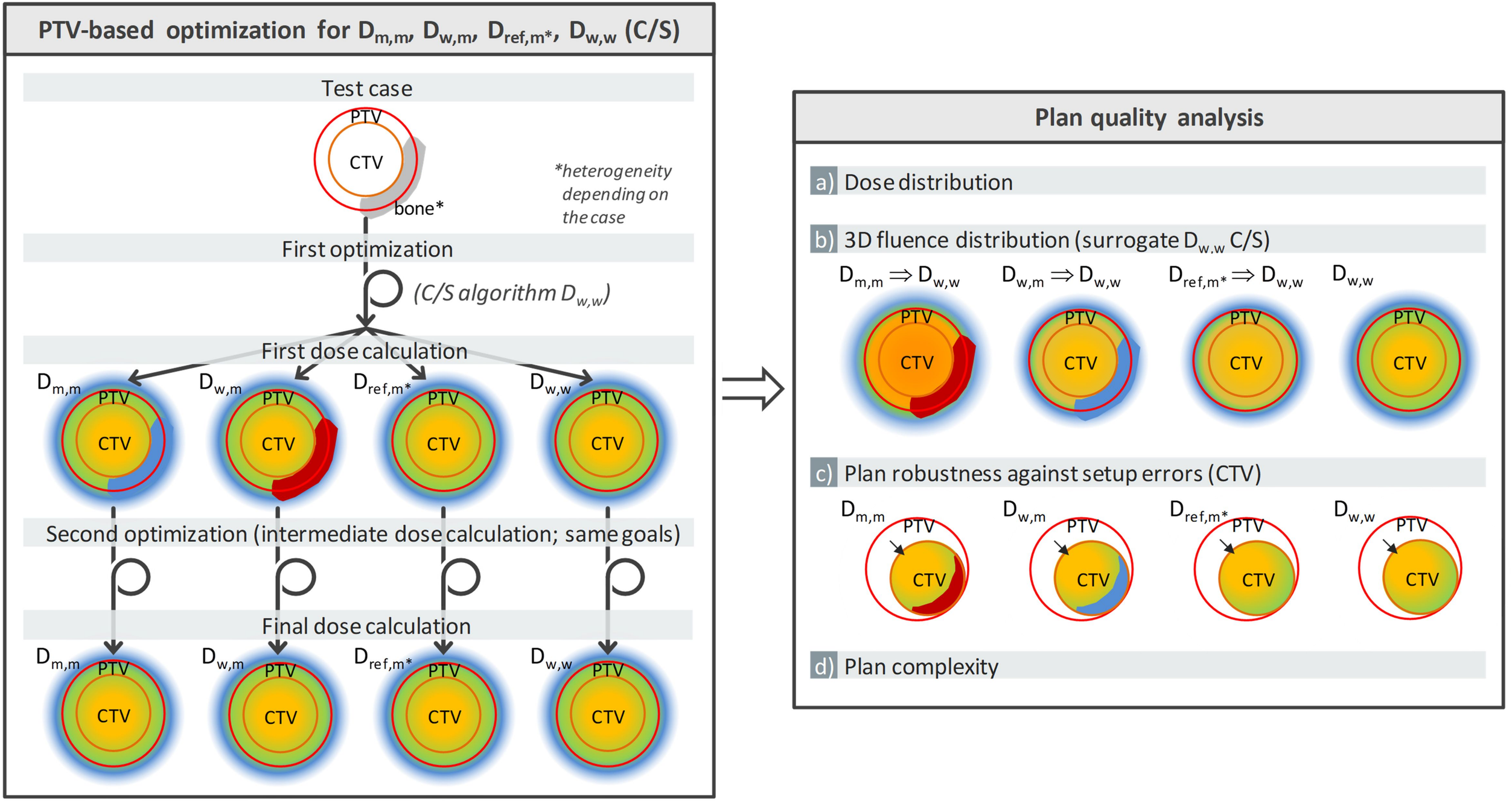
PTV-based optimization for $D_{m,m}$, $D_{w,m}$, $D_{ref,m*}$, $D_{w,w}$ (C/S)
Test case
PTV
CTV
bone*
*heterogeneity depending on the case
First optimization
(C/S algorithm $D_{w,w}$)
First dose calculation
$D_{m,m}$
$D_{w,m}$
$D_{ref,m*}$
$D_{w,w}$
Second optimization (intermediate dose calculation; same goals)
Final dose calculation
Plan quality analysis
a) Dose distribution
b) 3D fluence distribution (surrogate $D_{w,w}$ C/S)
$D_{m,m} \Rightarrow D_{w,w}$
$D_{w,m} \Rightarrow D_{w,w}$
$D_{ref,m*} \Rightarrow D_{w,w}$
$D_{w,w}$
c) Plan robustness against setup errors (CTV)
d) Plan complexity

(a)

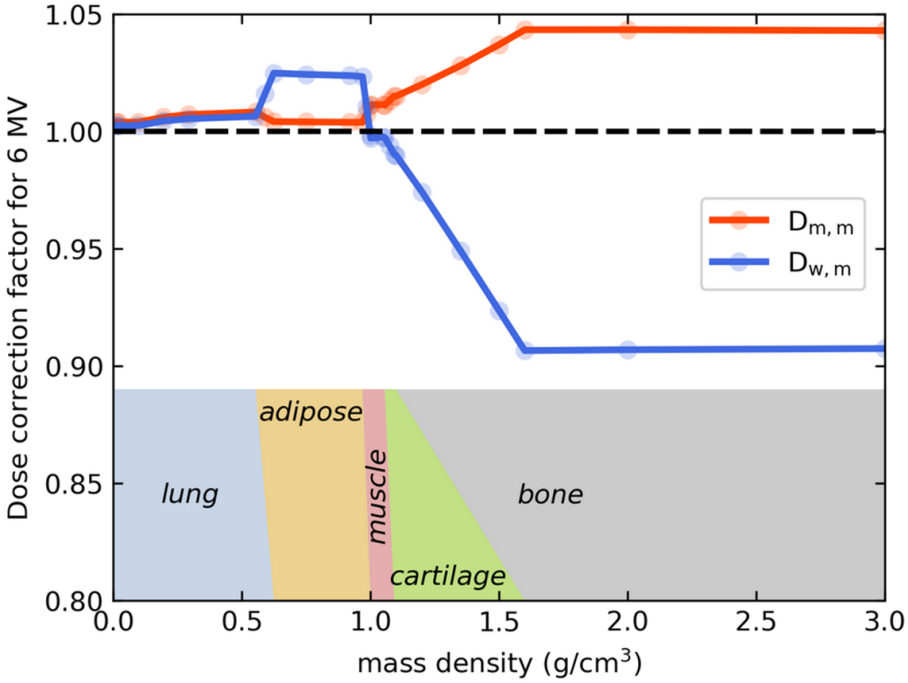


(b)

| Mass density (g/cm$^3$) | | | $CF_{mAXB}^{6MV}$ | |
|---|---|---|---|---|
| Minimum | Maximum | Material | $D_{m,m}$ | $D_{w,m}$ |
| 0.0000 | 0.5539 | Lung | 1.007 | 1.005 |
| *0.5539* | *0.6242* | *overlap (linear interpolation)* | | |
| 0.6242 | 0.9693 | Adipose | 1.007 | 1.024 |
| *0.9693* | *1.0010* | *overlap (linear interpolation)* | | |
| 1.0010 | 1.0556 | Muscle | 1.011 | 0.997 |
| *1.0556* | *1.0931* | *overlap (linear interpolation)* | | |
| 1.0931 | 1.1000 | Cartilage | 1.015 | 0.990 |
| *1.1000* | *1.6000* | *overlap (linear interpolation)* | | |
| 1.6000 | 3.0000 | Bone | 1.043 | 0.907 |
| - | - | Titanium alloy | 1.100 | 0.685 |

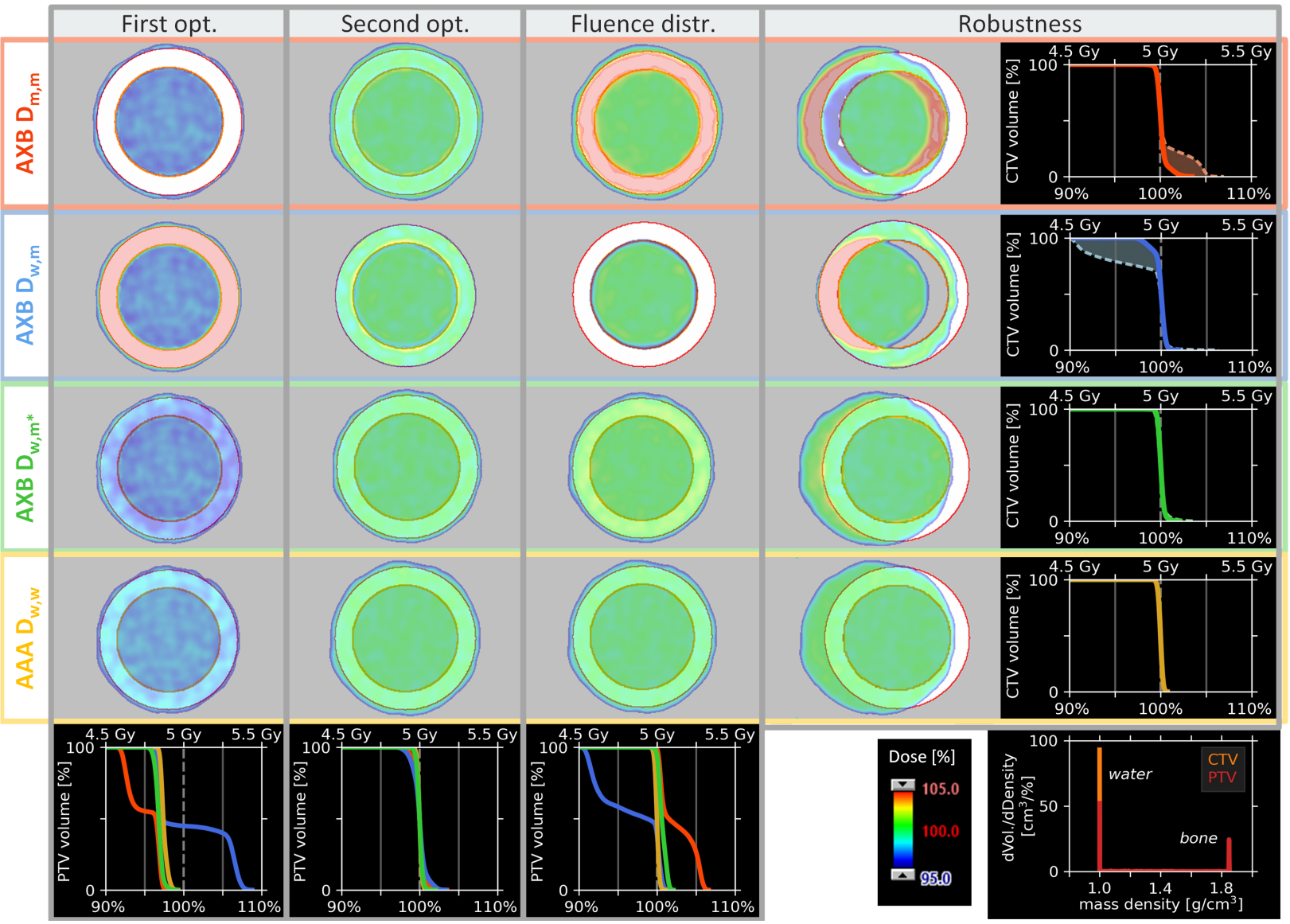
First opt.
Second opt.
Fluence distr.
Robustness
AXB $D_{m,m}$
AXB $D_{w,m}$
AXB $D_{w,m*}$
AAA $D_{w,w}$
CTV volume [%]
PTV volume [%]
4.5 Gy
5 Gy
5.5 Gy
100
0
90%
100%
110%
Dose [%]
105.0
100.0
95.0
dVol./dDensity [cm³/%]
water
bone
CTV
PTV
1.0
1.4
1.8
mass density [g/cm³]

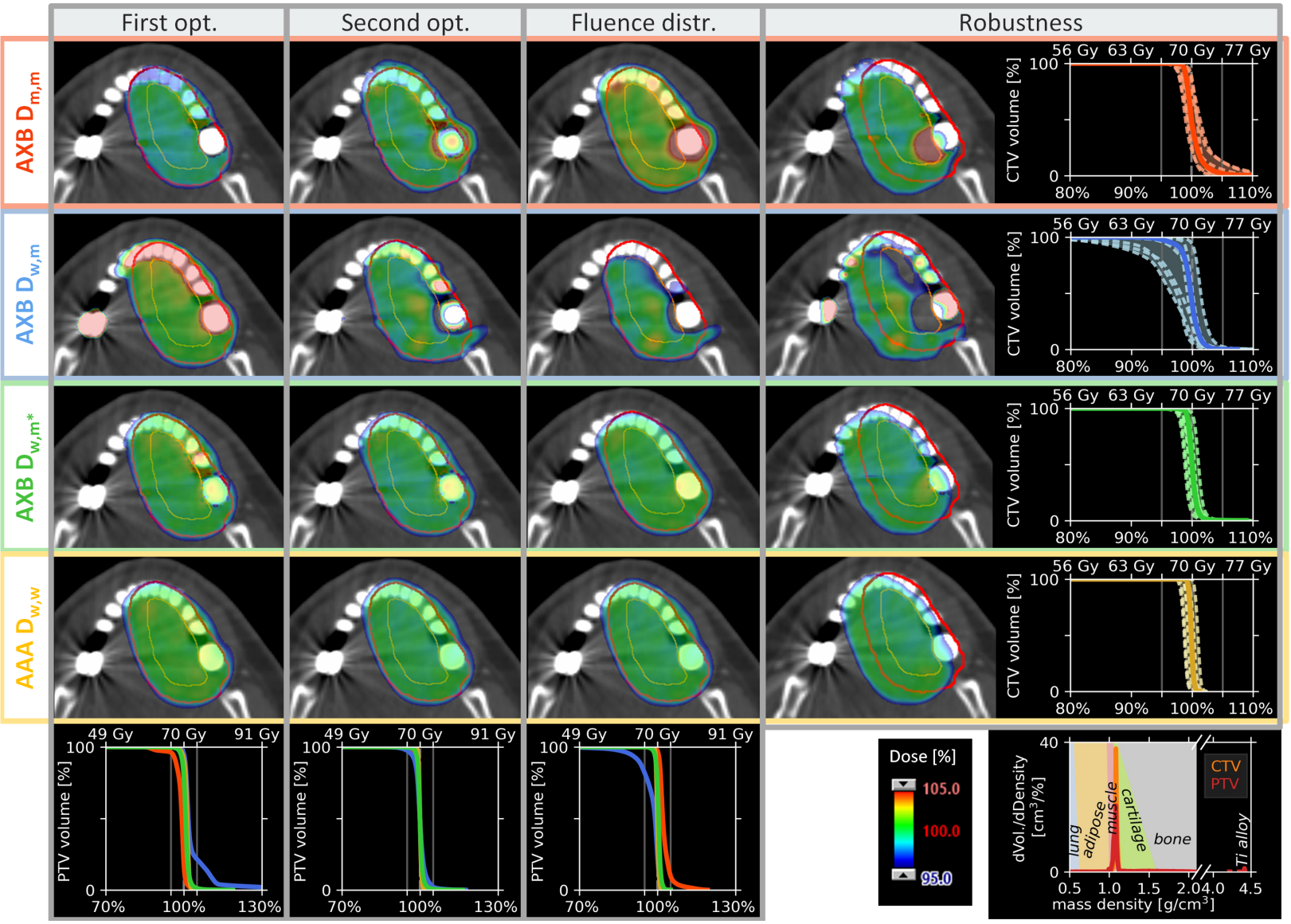
First opt.
Second opt.
Fluence distr.
Robustness
AXB $D_{m,m}$
AXB $D_{w,m}$
AXB $D_{w,m^*}$
AAA $D_{w,w}$
CTV volume [%]
56 Gy 63 Gy 70 Gy 77 Gy
100
0
80% 90% 100% 110%
PTV volume [%]
49 Gy 70 Gy 91 Gy
70% 100% 130%
Dose [%]
105.0
100.0
95.0
dVol./dDensity [cm³/%]
40
0
lung
adipose
muscle
cartilage
bone
Ti alloy
CTV
PTV
0.5 1.0 1.5 2.0 4.0 4.5
mass density [g/cm³]

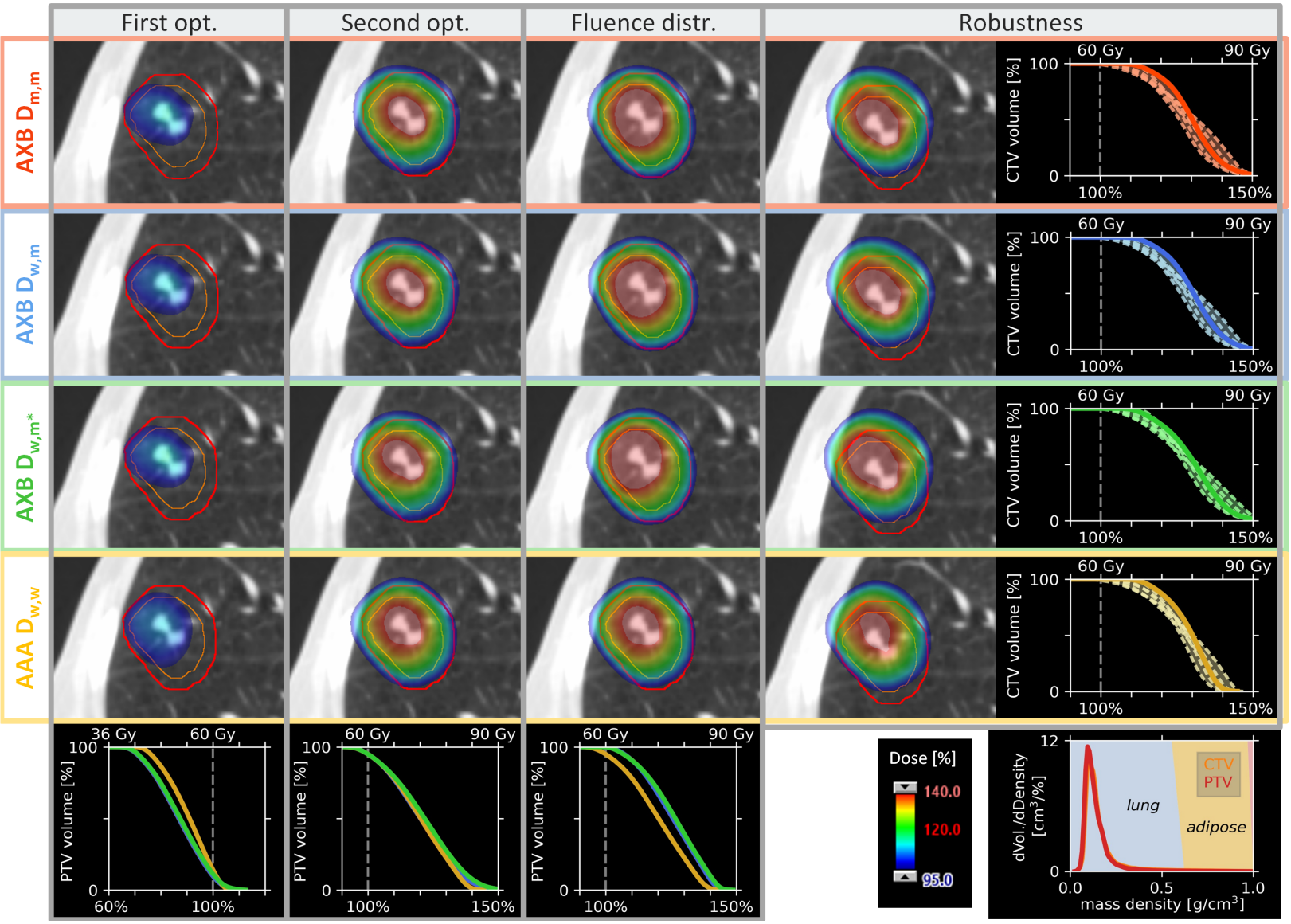
First opt.
Second opt.
Fluence distr.
Robustness
AXB $D_{m,m}$
AXB $D_{w,m}$
AXB $D_{w,m^*}$
AAA $D_{w,w}$
CTV volume [%]
60 Gy
90 Gy
100
0
100%
150%
PTV volume [%]
36 Gy
60 Gy
60%
Dose [%]
140.0
120.0
95.0
dVol./dDensity [cm³/%]
CTV
PTV
lung
adipose
12
0.0
0.5
1.0
mass density [g/cm³]

(a)

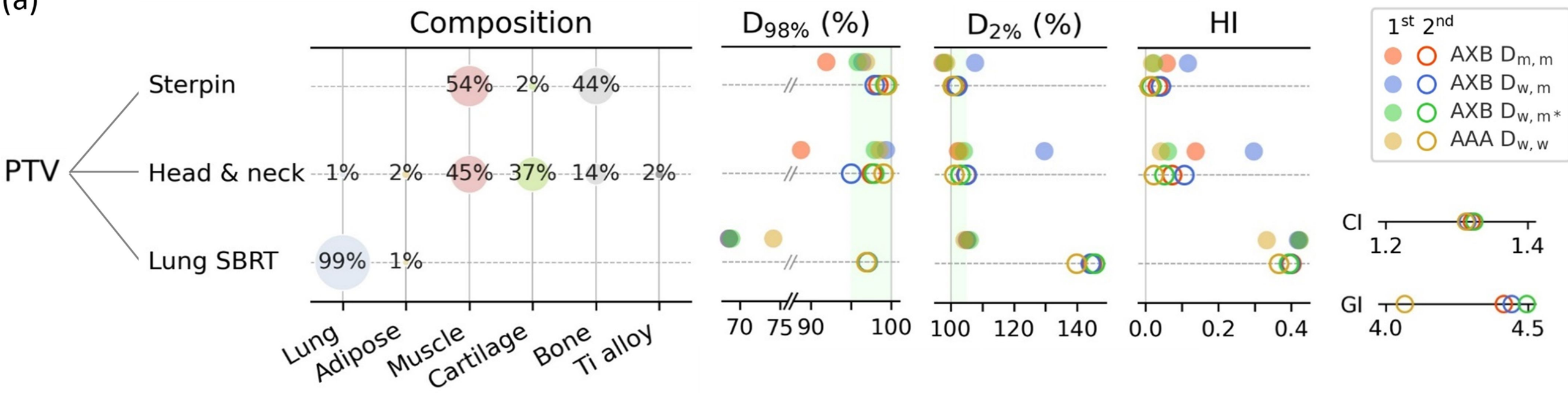
PTV
Sterpin
Head & neck
Lung SBRT
Composition
54% 2% 44%
1% 2% 45% 37% 14% 2%
99% 1%
Lung
Adipose
Muscle
Cartilage
Bone
Ti alloy
D98% (%)
70 75 90 100
D2% (%)
100 120 140
HI
0.0 0.2 0.4
1st 2nd
AXB Dm, m
AXB Dw, m
AXB Dw, m*
AAA Dw, w
CI
1.2 1.4
GI
4.0 4.5

(b)

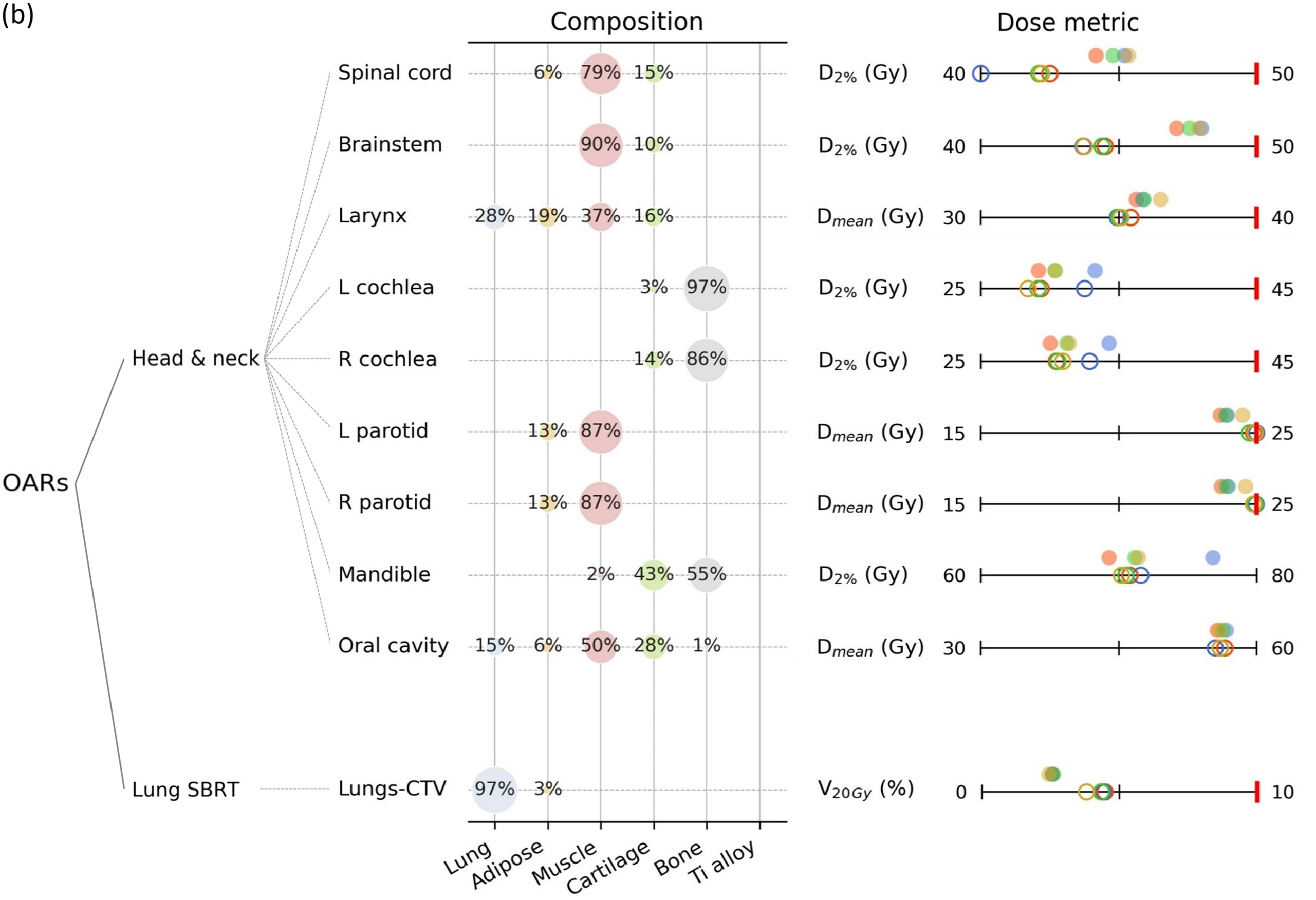
OARs
Head & neck
Lung SBRT
Spinal cord
Brainstem
Larynx
L cochlea
R cochlea
L parotid
R parotid
Mandible
Oral cavity
Lungs-CTV
6% 79% 15%
90% 10%
28% 19% 37% 16%
3% 97%
14% 86%
13% 87%
13% 87%
2% 43% 55%
15% 6% 50% 28% 1%
97% 3%
Lung
Adipose
Muscle
Cartilage
Bone
Ti alloy
Dose metric
D2% (Gy) 40 50
D2% (Gy) 40 50
Dmean (Gy) 30 40
D2% (Gy) 25 45
D2% (Gy) 25 45
Dmean (Gy) 15 25
Dmean (Gy) 15 25
D2% (Gy) 60 80
Dmean (Gy) 30 60
V20Gy (%) 0 10

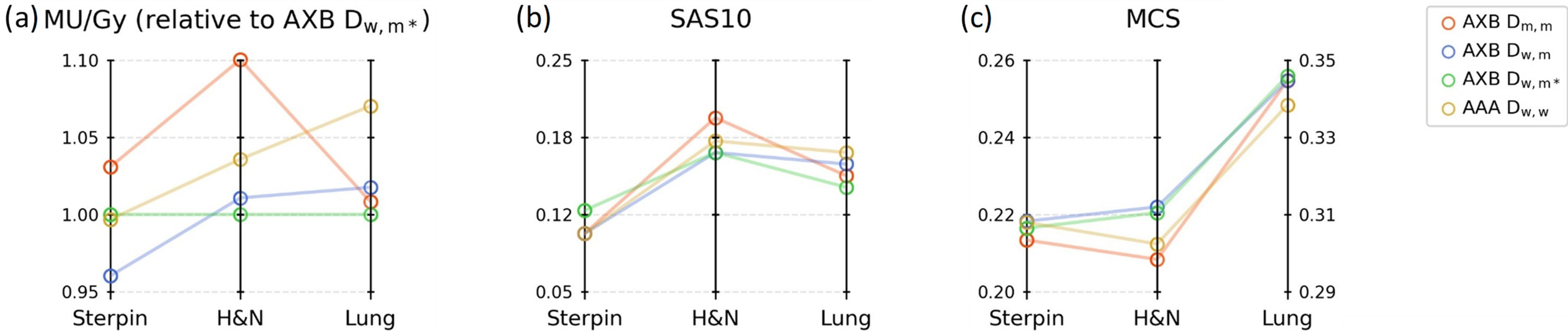
(a) MU/Gy (relative to AXB $D_{w,m*}$)
1.10
1.05
1.00
0.95
Sterpin
H&N
Lung
(b) SAS10
0.25
0.18
0.12
0.05
Sterpin
H&N
Lung
(c) MCS
0.26
0.24
0.22
0.20
0.35
0.33
0.31
0.29
Sterpin
H&N
Lung
AXB $D_{m,m}$
AXB $D_{w,m}$
AXB $D_{w,m*}$
AAA $D_{w,w}$

TABLE I. Dose prescriptions, limits to organs-at-risk (OAR), and VMAT technique details. $V_{XGy}$ represents the volume receiving at least X Gy; $D_{X\%}$ corresponds to the dose covering X% of the volume; $D_{mean}$ is the volume mean dose.

| | Dose prescription | | OAR limits | | |
|---|---|---|---|---|---|
| Case | Structure | Dose/fractions | OAR | limit | VMAT arcs |
| Sterpin | PTV | 5 Gy/1 fr | - | - | 6 coplanar |
| Head and neck | PTV54 | 54 Gy/33 fr | Spinal cord | $D_{2\%} < 54$ Gy | 2 coplanar |
| | PTV60 | 60 Gy/33 fr | Brainstem | $D_{2\%} < 54$ Gy | |
| | PTV70 | 70 Gy/33 fr | Cochlae | $D_{2\%} < 45$ Gy | |
| | | | Larynx | $D_{mean} < 40$ Gy | |
| | | | Parotid glands | $D_{mean} < 25$ Gy | |
| Lung SBRT | PTV | 60 Gy/5 fr | Lungs minus ITV | $V_{20Gy} < 10\%$ | 6 half non-coplanar |

TABLE II. Variations of the dosimetric parameters for the CTV after the first and second optimizations. For each dose quantity, the percentage differences between the nominal scenario and the scenarios in which the parameter presented its minimum/maximum values are shown. The parameters $D_{X\%}$ correspond to the dose covering X% of the volume. Values that differed from those of the nominal scenario by more than 2% are in bold.

| | | CTV % difference after first optimization | | | | | | | | CTV % difference after second optimization | | | | | | | |
|---|---|---|---|---|---|---|---|---|---|---|---|---|---|---|---|---|---|
| | | AXB $D_{m,m}$ | | AXB $D_{w,m}$ | | AXB $D_{w,m*}$ | | AAA $D_{w,w}$ | | AXB $D_{m,m}$ | | AXB $D_{w,m}$ | | AXB $D_{w,m*}$ | | AAA $D_{w,w}$ | |
| Case | Parameter | min | max | min | max | min | max | min | max | min | max | min | max | min | max | min | max |
| Sterpin | $D_{98\%}$ | 0.0 | 0.7 | 0.0 | 0.0 | 0.0 | 0.1 | 0.0 | 0.0 | -0.1 | 0.0 | **-7.5** | 0.0 | -0.2 | 0.0 | -0.1 | 0.0 |
| | $D_{50\%}$ | 0.0 | 0.0 | 0.0 | 0.0 | 0.0 | 0.0 | 0.0 | 0.0 | 0.0 | 0.1 | -0.2 | 0.0 | -0.1 | 0.0 | 0.0 | 0.0 |
| | $D_{2\%}$ | 0.0 | 0.1 | -0.8 | 0.0 | 0.0 | 0.7 | 0.0 | 0.0 | 0.0 | **3.1** | 0.0 | 0.4 | 0.0 | 0.7 | 0.0 | 0.0 |
| Head and neck | $D_{98\%}$ | -1.5 | 1.0 | -1.3 | 0.8 | -1.4 | 0.9 | -1.6 | 0.9 | -1.8 | 0.3 | **-16.6** | 1.6 | -1.9 | 0.6 | -1.5 | 1.0 |
| | $D_{50\%}$ | -1.1 | 0.9 | -1.2 | 1.0 | -1.1 | 1.0 | -1.2 | 0.9 | -1.0 | 1.4 | **-3.3** | 1.6 | -1.2 | 1.1 | -1.2 | 1.1 |
| | $D_{2\%}$ | -0.9 | 1.2 | -1.5 | 1.3 | -0.9 | 1.2 | -1.3 | 0.9 | **-2.9** | **6.6** | -1.7 | **2.6** | -1.0 | 1.4 | -0.9 | 1.2 |
| Lung SBRT | $D_{98\%}$ | **-7.2** | 0.9 | **-7.2** | 0.9 | **-7.2** | 0.9 | **-7.1** | 0.5 | **-9.9** | 0.0 | **-9.8** | 0.0 | **-9.9** | 0.7 | **-11.3** | 0.0 |
| | $D_{50\%}$ | **-2.5** | 0.0 | **-2.5** | 0.0 | **-2.6** | 0.0 | **-2.4** | 0.0 | **-4.3** | 1.5 | **-4.4** | 1.3 | **-4.4** | 0.5 | **-3.9** | 0.3 |
| | $D_{2\%}$ | **-1.9** | 1.2 | **-1.9** | 1.8 | **-2.0** | 1.3 | **-2.1** | **3.3** | **-3.2** | 1.7 | -1.3 | 2.0 | **-2.7** | 1.6 | **-2.9** | **3.5** |